

RHESSI OBSERVATIONS OF THE SIZE SCALES OF SOLAR HARD X-RAY SOURCES

E. J. SCHMAHL¹ and G. J. HURFORD²

¹*Astronomy Department, University of Maryland, College Park, 20742, U.S.A.;*
e-mail: edward.schmahl@gsfc.nasa.gov,

²*Space Sciences Laboratory, University of California, Berkeley, CA 94720-7450, U.S.A.*

(Received 7 August 2002; accepted 3 September 2002)

Abstract. The Reuven Ramaty High-Energy Solar Spectroscopic Imager RHESSI telescope produces hard X-ray images by Fourier imaging techniques that are capable of determining the sizes and shapes of sources with spatial scales in the range $\sim 2''$ – $180''$. Applying the method of Unpixelized Forward Fitting to RHESSI modulation profiles from simple flares, we have identified the presence of ‘halo’ sources whose size scale ($\sim 40''$) greatly exceeds the ‘core’ sizes ($\leq 6''$ – $14''$). Although such ‘core-halo’ structures have been observed at radio wavelengths using a similar technique, the radio and hard X-ray phenomena may be different. These observations raise questions about the nature of these ‘halos’. Among the possibilities are that they are albedo sources, thin-target loops, or unidentified diffuse structures.

1. Introduction

The primary scientific objective of the Reuven Ramaty High-Energy Solar Spectroscopic Imager (RHESSI) is the study of energy release and particle acceleration in solar flares. This is achieved by imaging-spectroscopy of solar hard X-rays and gamma-rays over a 3-keV to 17-MeV energy range using a set of nine Rotating Modulation Collimators (RMCs) with high-purity germanium detectors. The scientific objectives, instrument and associated imaging techniques are described in detail by Lin *et al.* (2002), Smith *et al.* (2002), and Hurford *et al.* (2002) earlier in this volume.

As described by Hurford *et al.* (2002), the rotation of the spacecraft modulates the detected count rates from the incident hard X-rays, so that the amplitudes and phasing of the observed sinusoid-like time profiles (modulation profiles) provide information on the positions, sizes and shapes of hard X-ray sources. RHESSI’s imaging method is precisely analogous to that of earth rotation synthesis in radio interferometry, with collimation replacing interference and spacecraft rotation replacing Earth rotation.

Clearly, the measurement of source size scales and morphology is relevant to determining the properties of the electron acceleration region and for constraining models of the acceleration process. With this in mind, we have selected several RHESSI flares with simple shapes and time profiles for which the size scales can



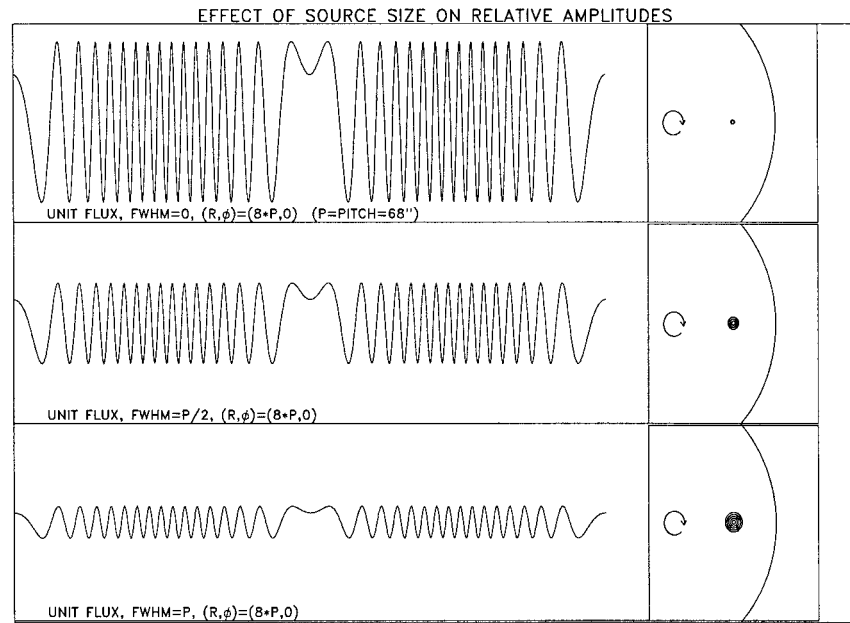


Figure 1. Ideal modulation profiles as a function of source diameter.

be most accurately determined, and have applied forward-fitting methods to the light curves to obtain sizes and spatial profiles of the hard X-ray sources.

2. Sizes and Relative Amplitudes

The amplitude of the modulation profile depends on the flux and the extent of the source, as well as on instrumental parameters such as the grid transmission and the detector sensitivity. The use of the relative amplitude – defined as the ratio of the modulation amplitude to the mean flux – removes the dependence on flux and detector response and so can directly measure the source extent in the direction perpendicular to the slits. (This assumes that background is negligible.) Wider sources produce smaller relative amplitudes. This is illustrated in Figure 1. For a Gaussian source with $\text{FWHM} = \Delta\theta$ the relative amplitude decreases with decreasing resolution $\Delta\theta_{\text{res}}$ as $\exp(-0.89(\Delta\theta/\Delta\theta_{\text{res}})^2)$. In general, for any assumed profile (e.g., Gaussian, pillbox or capped power law), the relative amplitude can be computed by taking the Fourier transform of the profile. Conversely, if the relative amplitude is known at a sufficient number of wavenumbers ($2\pi/\text{angular pitch}$), the profile can be found by computing the inverse transform of the relative amplitude.

For an RMC like RHESSI, the fundamental component of the response to a point source is a sinusoidal function of source position, with suitable modifications for the slowly varying grid transmission and effective slit/pitch ratios. The

instantaneous response to a point source may be represented by the following equation:

$$C_{pt} = F_0 \mathcal{G}(\phi) [1 + \mathcal{M}(\phi) \cos(2\pi(ux + vy) - \Phi)]. \tag{1}$$

In this expression, F_0 is the flux of the point source at the time where the slit angle (also the wave number angle) = ϕ , $\mathcal{G}(\phi)$ is the grid transmission \times livetime at angle ϕ , $\mathcal{M}(\phi)$ is the maximum modulation amplitude, and Φ is the instantaneous phase at map center determined by the aspect system. If the instantaneous responses (1) are added together in (x, y) space with appropriate weighting over one rotation, one gets a Bessel function profile ($J_0(kr)$) representing the RHESSI point response as a function of radius, r .

By the principle of superposition, an extended source with a brightness distribution $I(x, y)$ can be represented as a sum of point sources around the centroid (x_0, y_0) , so that the count modulation profile (C_{ext}) may be represented as a sum of expressions like Equation (2). Therefore the extended instantaneous response becomes:

$$C_{ext} = F_0 \int \int I(x, y) \{ \mathcal{G}(\phi) [1 + \mathcal{M}(\phi) \cos(2\pi(ux + vy) - \Phi)] \} dx dy. \tag{2}$$

Note that any such (x, y) sum over sinusoids, $\cos(ux + vy - \Phi)$, is another sinusoid with different amplitude, and possibly different phase:

$$C_{ext} = F_0 \{ \mathcal{G}(\phi) [1 + \rho(\phi) \mathcal{M}(\phi) \cos(2\pi(ux_0 + vy_0) - \Phi')] \}, \tag{3}$$

where

$$\rho(\phi) = \frac{\int \int I(x, y) \cos(2\pi(ux + vy) - \Phi) dx dy}{\int \int I(x, y) dx dy}. \tag{4}$$

In this expression, $\rho(\phi)$ is the relative amplitude, which is always ≤ 1 , and Φ' is a phase-shifted version of Φ . For symmetric distributions $I(x, y)$ whose centroid is at the map center, $\Phi' = \Phi$ (no phase shift).

Figure 2 shows relative amplitudes produced by simple symmetric functions. We have selected three profiles illustrative of a range of behavior: very compact (pillbox), moderately compact (Gaussian), and extended (capped powerlaw):

- (1) Pillbox: $I(r) = 1$ for $r \leq a$ and 0 otherwise;
- (2) Gaussian: $I(r) = \exp(-\frac{1}{2}(r/a)^2)$;
- (3) Capped power law: $I(r) = [(r/a)^2 + 1]^{-3/2}$, $\rightarrow r^{-3}$ for $r \gg a$ and $\rightarrow 1$ for $r \ll a$.

Figure 2 shows that the more compact the source, the narrower the profile of relative amplitudes, and *vice versa*. Note that even though the capped power-law (medium) and Gaussian (light) intensity profiles are similar out to their FWHM,

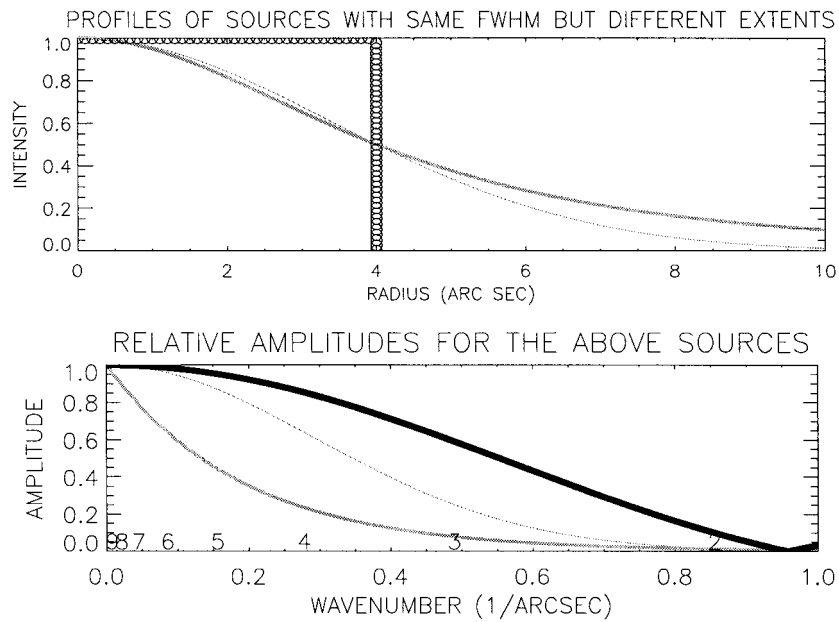


Figure 2. Relative amplitudes for representative simple, symmetric functions: a round pillbox (*thick*), a Gaussian (*light*) and a ‘capped power-law’ intensity profile (*medium width*). The latter corresponds to an exponential relative amplitude profile, ($\exp(-ka)$). The numbers above the abscissa identify the RHESSI subcollimators which measure the corresponding wavenumbers.

the extended tail (representing a ‘halo’) of the capped power-law intensity profile causes a big difference in the relative amplitude at low wave numbers. This demonstrates the ability of Fourier methods to identify and characterize extended sources.

3. Observed Relative Amplitudes

3.1. CANDIDATE FLARES – SIMPLE, STEADY, AND STRONG

Since our objective is to determine sizes and spatial profiles of HXR flares, we have focused on simple, steady and strong events.

Using the RHESSI CLEAN algorithm (see Hurford *et al.*, 2002, for details), we mapped ~ 40 flares, and selected those that satisfy the following criteria:

- (1) The source consists of a single component.
- (2) The flux is steady to $\lesssim 10$ percent over a rotation (~ 4 s).
- (3) The source is relatively ‘round’ (axial ratio $\lesssim 1.25$).
- (4) The count rate in the 12–25 keV band is > 500 counts $\text{s}^{-1}\text{SC}^{-1}$.

After this filtering of the database, we were left with seven events, whose CLEAN maps are shown in Figure 3. We include only subcollimators 3–9 in our study. We excluded 1 and 2, since the threshold of detector 2 is set to ~ 20 keV (compared to

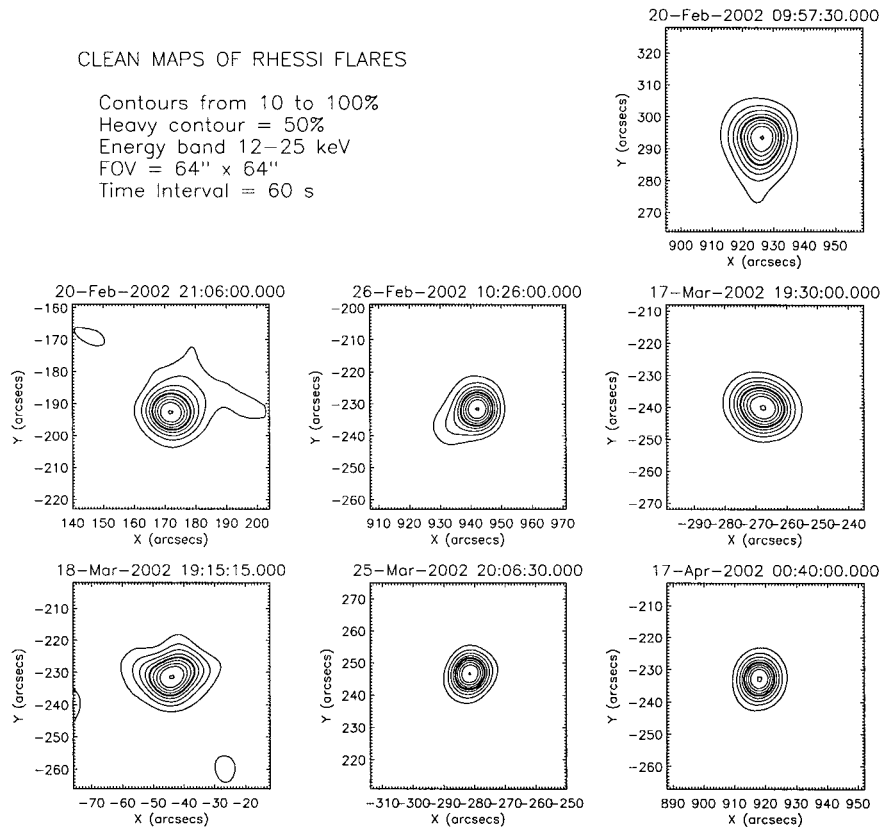


Figure 3. CLEAN maps of flares used in this study (UT times). The field of view in each map is $64'' \times 64''$, and the maps were made using subcollimators 3 ($7''$ resolution) through 8 ($105''$ resolution).

our 12–25 keV analysis band) and since subcollimators 1 and 2 have only recently been self-calibrated in phase (June 2002). Subsequent studies will include 1 and 2, since their higher spatial resolutions can provide quite important information.

3.2. MODULATION PROFILES

Since the modulation frequency increases systematically with higher spatial frequency of the grids, grouping the observed counts into overly coarse time bins could preferentially reduce the modulation amplitude at higher spatial frequencies. For this reason, we used relatively short time bins of 1 ms so as to reduce the worst-case loss of modulation amplitude to less than 0.5% for grids 5 through 9 and less than 3% for grids 3 and 4. Average reductions would be less than these limits.

With such small time bins, most of the flares in our sample produce mean count rates of only a few counts per time bin, and Poisson fluctuations are quite signif-

icant. This is not a problem for our analysis, which is not as sensitive to Poisson fluctuations as other algorithms (e.g., Pixelized Forward Fitting) may be.

It is important to note that the use of the C-statistic is essential to obtaining a proper fit, since there tend to be fewer than 10 counts per time bin (Cash, 1979; and Aschwanden *et al.* this volume.) The χ^2 statistic leads to erroneous results with small time bins, and so it was not used. Valid results were also obtained by minimizing the r.m.s. deviation of the model from the data.

Figure 4 shows four of the modulation profiles during a 4 s interval for one of the events compared to a fit (Equation (3)) for parameters derived from forward-fitting. The method for fitting the model is quite straightforward since the flares are fairly round and constant so that the only time dependence is due to modulation. To start off, guesses are input for (x, y) on a 2-D grid with increments of $\frac{1}{8}$ the current angular pitch. For each (x, y) , flux values (F_0) and relative amplitudes (ρ) are found by minimizing the least squares fit of the function (3). After the minimum C-statistic is found, the values for x, y, F_0 , and ρ are used for a second-order search using the amoeba method.

Background is not important in these events, as confirmed by inspecting the flux profile. However, there are random data gaps caused by cosmic rays within these profiles, and measures have been taken to exclude the gaps from the analysis. More than $\sim 99\%$ of the gaps have a characteristic signature (Smith *et al.*, 2002) so that once identified, they can be flagged and excluded from subsequent analysis.

4. Sizes, Profiles and ‘Core-Halos’

4.1. FAILURE OF SINGLE GAUSSIANS

Figure 5 shows the relative amplitude spectra $\rho(k)$ determined for the seven flares. The curves fitted to the data points are functions of the form $\log(\rho) = ak^b$. When $b = 2$, the source is a Gaussian, a traditional shape used in physics and astronomy, and in particular, solar physics, to characterize partially resolved sources (e.g., *Yohkoh/HXT*, microwave, mm-wave observations and the Forward-Fitting method used by the RHESSI software – Aschwanden *et al.*, 2002.) In our case, the fits indicate non-Gaussian shapes, and $b \approx 1$, implying a e^{-kr} dependency. Gaussians that fit the first and last points are shown by the dotted curves, which in most cases are a poor fit to the data.

4.2. PROFILE BY INVERSION

As mentioned earlier, relative amplitude spectra with sufficient wavenumber coverage may be Fourier back-transformed to provide intensity profiles of the source without making *a priori* assumptions about their functional form. Using interpolation between the data points, we have inverted the spectra to obtain profiles. Since the relative amplitude spectra were obtained under the assumption of azimuthal

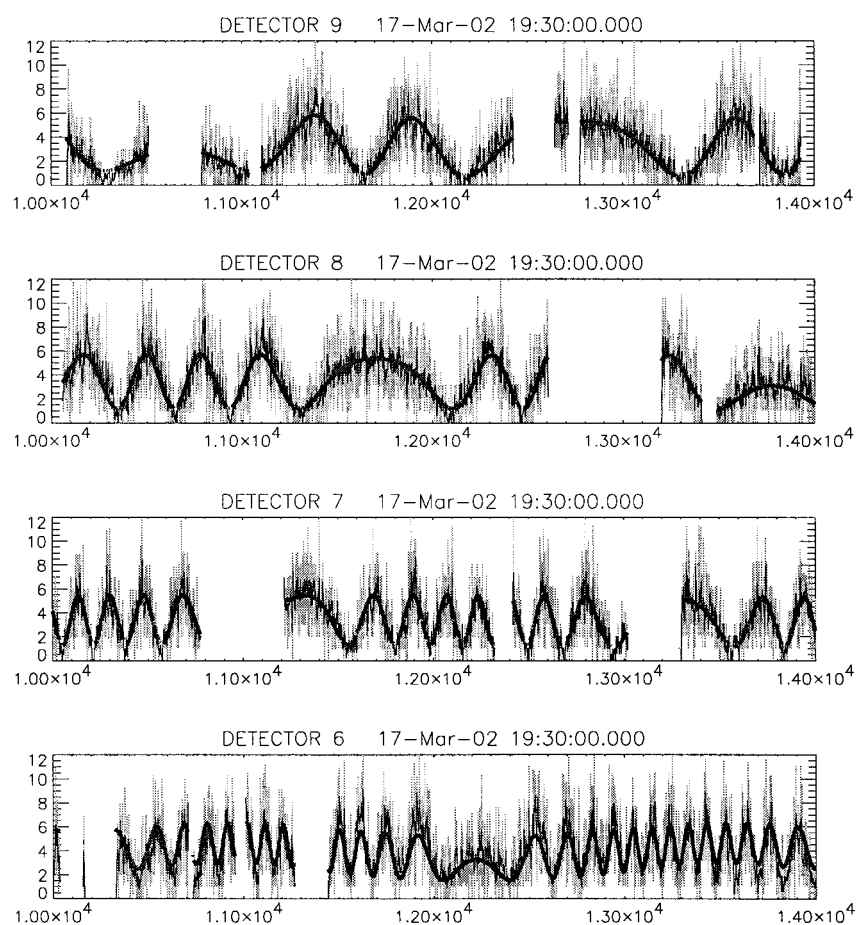


Figure 4. Modulation profiles for one rotation of the 17 March 2002 event for the 4 coarsest subcollimators, 6, 7, 8, and 9 whose cycles are sufficiently long that modulation is visible to the eye in the printed format available (UT times). The *thin, gray, jagged curves* are the count profiles (counts per time bin) and the *smooth, dark curves* are the 4-parameter fits using Equation (3). Inspection of the fitted curve for subcollimator 9 shows that the curves drop relatively close to the time axis, which indicates that the relative amplitude is nearly 1. For subcollimators 8, 7, and 6, the ratio of the amplitudes of the modulation to their means decreases as the angular pitch decreases, indicating that the relative amplitude decreases with increasing wave number. (Accurate determination of the relative amplitude requires corrections for the known effects of internal shadowing in the grids, and cannot be done by eye from this figure.) Similar effects may be seen in the plots of all the data and the fitted curves in the CD-ROM provided with this issue.

symmetry, the two-dimensional Fourier transforms reduce to pairs of Bessel transforms:

$$\rho(k) = \int I(r) J_0(kr) r dr, \quad (5)$$

FITS OF RELATIVE AMPS TO
 $\log \rho = a k^b$
 Goodness of fit measured by
 $\sigma = \text{RMS deviation}$.
 $b=1$ implies powerlaw,
 $b=2$ implies gaussian

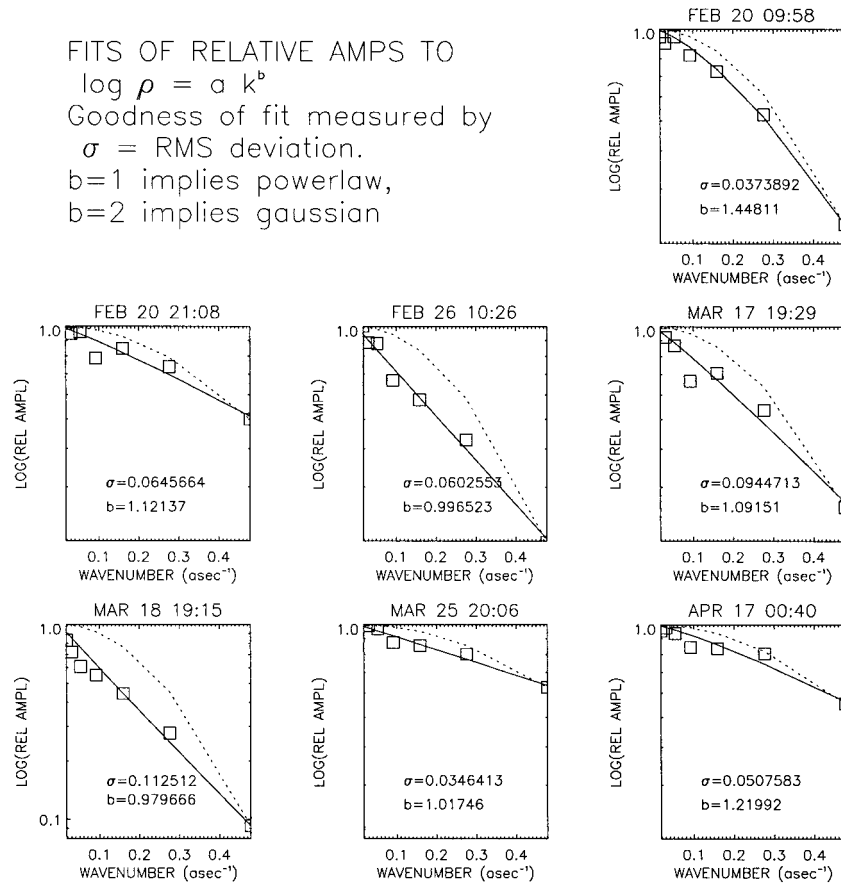


Figure 5. Subcollimator-to-subcollimator relative amplitude spectra (UT times). The *squares* are the measured values of $\rho(k)$ and the *solid curves* show fits with a power function ak^b . The index b , and a measure of goodness of fit, $\sigma = \text{r.m.s. deviation}$, are shown in each plot. The *dotted curves* are for Gaussians, which are poor fits to the data.

$$I(r) = \int \rho(k) J_0(kr) k dk. \quad (6)$$

The results of applying Equation (6) to the interpolated $\rho(k)$ spectra are shown in Figure 6. The spectra have been lightly tapered by a hyperbolic tangent function because most of the spectra do not fall off to small values at the largest k (≈ 0.5) for subcollimator 3. This smooths out the ‘ringing’ effect caused by abruptly truncating the spectra. Data for subcollimators 1 and 2 would extend the domain to higher k values, and presumably lower ρ values, and negate the need for tapering. In any event, tapering has no effect on the finding of ‘halos’.

Although the profiles shown in Figure 6 appear remarkably like Gaussians, this is simply the result of the use of a linear display. Any broadly extended source several times the diameter of the core sources would have a low surface brightness

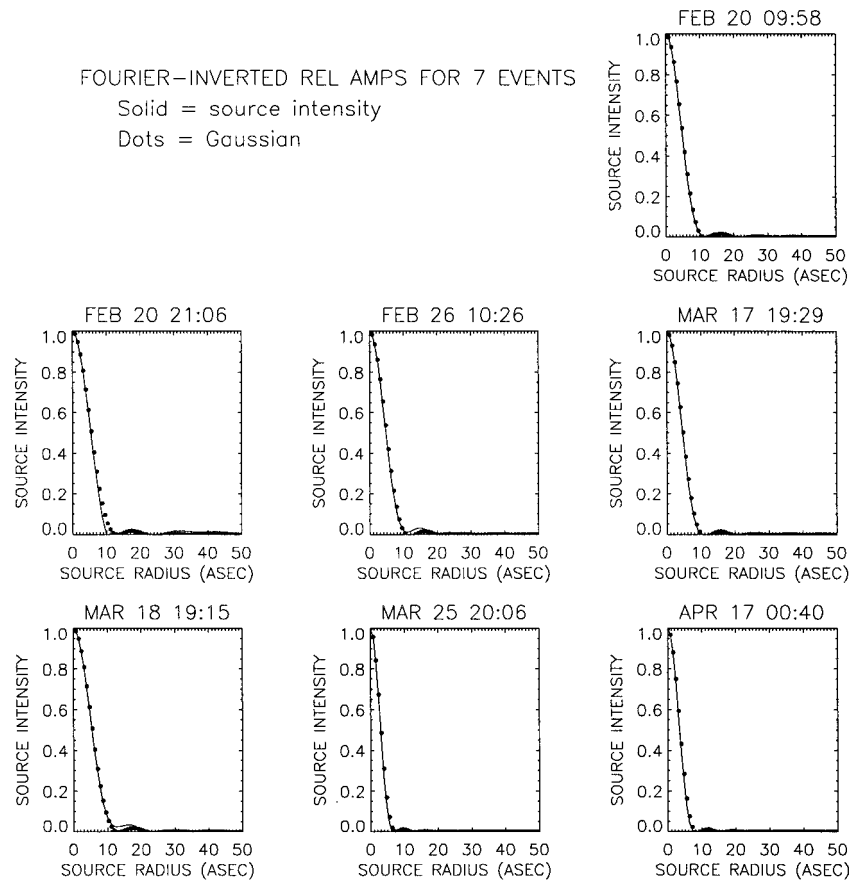


Figure 6. Core intensity profiles from inverted relative amplitude spectrum (UT times). The plots show the intensity profiles obtained by Fourier inversion using Equation (6) for the 7 flares. These are well fit by Gaussians (*dotted curves*). But, in common with other pixelized methods, they do not show all the flux. (Compare with the flux curves in Figure 7.)

that cannot be seen either in Figure 6 or in the maps in Figure 3. To get around this difficulty, we plot the cumulative flux from radius, r , to ∞ as a function of r . For a pure Gaussian, this is again a Gaussian. But Figure 7 shows that for most of the 7 events there is substantial flux (10–30%) in an extended region beyond 5–10 arc sec from the center. This appears as a broad ‘tail’ in the flux profile.

One of the flux profiles, for the 20 February 21:06 event, shows a positive slope near 10–20'', which cannot be real. Inspection of the relative amplitude profile for this flare (Figure 5) shows that it is far from smooth, and the value for subcollimator 6 (at wave number = 0.09) appears to be an ‘outlier’ from the trend of the data. The low value of relative amplitude in this particular instance causes negative values to appear around 10–20'' in the transform of the profiles, and this leads to a region of positive slope in the cumulative flux curve for this event (Figure 7). The other flares

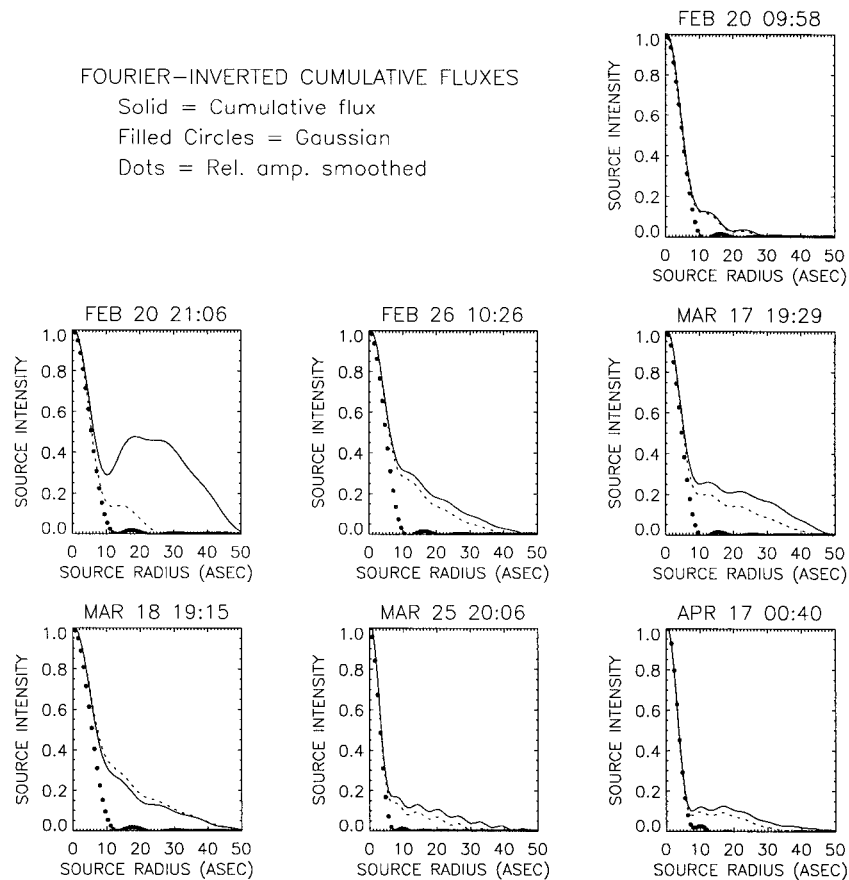


Figure 7. Cumulative fluxes from inverted relative amplitude spectra (UT times). The plots show the cumulative flux profiles $\int_r^\infty r I(r) dr$ for the same inverted data shown in Figure 6. In all cases the profiles are Gaussian-like in the core, very much like in Figure 6, but extended beyond the FWHM.

do not exhibit this behavior, and it may be significant that the CLEAN map of this particular flare differs from the others in its shape at low levels. The CLEAN map (Figure 3) shows an extended long feature, which either contributes to this anomaly in relative amplitudes at the spatial scale of subcollimator 6 ($\sim 36''$) or illustrates some difficulties in CLEANing at the 10–20% level.

To see how ‘noise’ (or outliers) in the trends of relative amplitudes can affect the cumulative flux curves, we have smoothed the relative amplitude profiles before doing the transforms. The dotted curves in Figure 7 show the effect of smoothing. In the case of the 20 February 21:06 UT flare, smoothing eliminates the anomalous positive slope and reduces the ‘halo’ flux by about a factor of 2. For the other cumulative flux curves (none of which have significant positive slopes), the effects of smoothing are minimal, a few percent, either positive or negative.

5. Tests and Cross Checks

5.1. ANALYTIC TESTS

To check that the algorithm used here to find the relative amplitudes works correctly, we have tested it with a simulation in which the RHESSI count rate profiles are replaced by functions of the form

$$C_{\text{sim}} = F_0 \mathcal{G}(\phi) [1 + \mathcal{M}(\phi) \cos(2\pi(ux + vy) - \Phi)], \quad (7)$$

where Φ is the observed array of phases at map center, u and v are the arrays of points (on circles) given by the roll angles and angular pitches for the selected event; \mathcal{G} and \mathcal{M} are found from the standard RHESSI mapping software for the time and location of the flare. Then F_0 , ρ , x , and y were found. The resulting fits were exact to machine accuracy, as expected since there was no noise or Poisson fluctuations.

5.2. POISSON SIMULATIONS

In the next test, a Poisson-distributed function replaced the count rates, where the IDL Poisson-distribution generator created a sample using the mean value of the model in each time bin. The resulting fits were excellent, indicating that Poisson fluctuations do not adversely affect the fits, even when the count rates are as low as ~ 1 count/time bin.

To check that the fits using capped power laws or double superposed Gaussians were better than single Gaussians, we compared C-statistics. Fits with single Gaussian models always have a larger C-statistic.

5.3. POSSIBLE INSTRUMENTAL EFFECTS

The presence of the ‘halo’ components can be directly attributed to the relatively rapid falloff in relative amplitude at the low wavenumbers measured by the coarse subcollimators. Therefore it is appropriate to ask if there are any plausible instrumental effects that could cause such an effect.

5.3.1. Aspect System Errors

Imaging with RHESSI is directly dependent on knowledge of the pitch, yaw and roll aspect. Relative aspect errors during 21-s integrations would result in an image which represented a convolution of the source with the characteristics of these errors. To produce a spurious ‘halo’, such aspect errors would have to have a magnitude of 20 arc sec or larger. This is incompatible with continuous observations of the compact core and internal aspect redundancies that indicate an aspect solution that is self-consistent at the subarcsecond level (Fivian *et al.*, 2002). We conclude that aspect system performance is not an issue for this study.

5.3.2. *Modulation Amplitude Function*

Another possibility is that systematic errors in the modulation amplitude function $\mathcal{M}(\phi)$ (the multiplier of $\rho(\phi)$ in Equation (3)) could cause relative amplitudes to appear low if the values of $\mathcal{M}(\phi)$ were somehow too large. The same method is used to calculate the modulation functions for all grids, based on extensive preflight X-ray and optical calibrations of grid thickness, slat width, etc. There are three reasons for having confidence in the resulting values of $\mathcal{M}(\phi)$. First, the pre-flight calibrations were internally consistent at the $\sim 2\%$ level, giving us considerable confidence in the knowledge of the grid parameters. Second, calculations based on these parameters correctly account for the rotational variation of $\mathcal{M}(\phi)$ which is readily seen in the data. Third, for grids with slits and slats that are approximately equal, $\mathcal{M}(\phi)$ is relatively insensitive to the slit/slat ratio, which is itself accurately known.

5.3.3. *Grid Transmission*

Errors in the grid transmission function $\mathcal{G}(\phi)$ could lead to erroneous estimates of the relative amplitudes. The arguments in the foregoing paragraph also apply to this function. We conclude that it is highly unlikely that errors in either the grid transmission or modulation amplitude could account for the falloff in relative amplitude among the coarse grids.

5.3.4. *Background*

One other effect that can produce low relative amplitudes is background. In our flares, the pre-flare and post-flare fluxes in the flare time profiles were used to estimate background, which was at least two orders of magnitude below the peak flux in this energy band. Furthermore, there is no reason to expect the background errors to affect the detectors systematically as a function of the spatial frequency of their grids. Background can therefore be ruled out as a contributor to any errors in relative amplitude.

6. Discussion and Conclusions

The main result of this study is that Fourier techniques applied to seven RHESSI flares reveal extended features of low intensity. The surface brightness of these ‘halos’ is typically only $\sim 2\%$ or less than that of the core, so they are difficult to image with other methods. Nevertheless these ‘halos’ contain a significant fraction (10–30%) of the total flux. Table I shows the flare details, including the core size and the fractional flux of the extended features, as found from the point at which the tails of the profiles in Figure 7 depart from the Gaussian core.

We now consider possible explanations for the ‘halo’ features, and some ways by which their nature can be explored.

TABLE I
Properties of ‘core-halo’ events.

Date	Time	X-ray	Helio.	NOAA	Core	Halo
2002	(UT)	class	lat./long.	region	FWHM	flux
20 Feb.	09:58	M4.3	N18 W83	9825	10''	13%
20 Feb.	21:08	M2.4	S18 W11	9830	12''	12%
26 Feb.	10:26	C9.6	S13 W89	9830	12''	30%
17 Mar.	19:29	M4.0	S22 E16	9871	10''	25%
18 Mar.	19:15	C8.9	S21 E03	9871	14''	30%
25 Mar.	20:06	C9.8	N08 E17	9878	6''	16%
17 Apr.	00:40	C9.9	S13 W83	9905	7''	10%

The flux of Compton solar back-scattered X-rays, called albedo X-rays, can be as large as 25–50% of the primary X-rays in the 12–25 keV band (Alexander and Brown, 2002; Bai and Ramaty, 1978). The spatial distribution of albedo X-rays depends on the height and extent of the source X-rays, so examination of the albedo sources can, in principle, provide information about the height of the source. The center-to-limb dependence of the albedo is predicted by models and there should be discernible differences in the shape of the ‘halo’ at the limb as compared with near disk center. From the curves of Alexander and Brown, the relative flux of the albedo should be an increasing function of energy from 6 to ~ 40 keV, so the dependence of the relative amplitudes on energy should show this increase if the ‘halos’ are indeed albedo sources.

In the case of microwave flares containing ‘core-halo’ features, (e.g., Bastian, Benz, and Gary, 1998), the ‘halo’ is optically thin and polarized, while the core is optically thick and unpolarized. For gyrosynchrotron emission, this suggests that the core has a strong magnetic field and the ‘halo’ has a weaker one, compatible with the ‘halo’s’ extended nature. However, for the hard X-ray and radio ‘halos’ to be the same, the hard X-ray ‘halo’ would have to be due to thin-target emission from extended loops. In that case, one would expect the hard X-ray ‘halo’ to be stronger at lower energies. The reverse would be true if the ‘halo’ were an albedo source.

As RHESSI flares accumulate and the calibration and analysis software improve, this study will be extended to a wider range of energies and source morphologies. It should be possible to use such factors as energy- and limb-dependence to help identify the origin of the ‘halo’ sources and if they turn out to be albedo sources, this can be exploited to determine the heights of the primary, compact hard X-ray sources. Using the method we have outlined here, it may also be possible to provide good estimates for the the fractional contribution of the albedo component

in spectra on a flare-to-flare basis, thereby improving the interpretation of flare source spectra.

Acknowledgements

The authors thank Alicia Aarnio (NASA Goddard summer intern from Smith College) for mapping and CLEANing numerous candidate RHESSI flares for this study. One of the authors (EJS) acknowledges support by grant NAG-5-10180 from NASA Goddard Space Flight Center to the University of Maryland. The research is supported by NASA grant NAS5-98033-05/03.

References

- Alexander, R. C. and Brown, J. C.: 2002, *Solar Phys.*, this volume.
Aschwanden, M. J., Schmahl, E., and the RHESSI Team: 2002, *Solar Phys.*, this volume.
Bai, T. and Ramaty, R.: 1978, *Astrophys. J.* **219**, 275.
Bastian, T., Benz, A., and Gary, D.: 1998, *Ann. Rev. Astron. Astrophys.* **36**, 131.
Cash, W.: 1979, *Astrophys. J.* **228**, 939.
Fivian, M., Hemmeck, R., Mchedlishvili, A., and Zehnder A.: 2002, *Solar Phys.*, this volume.
Hurford, G. J. *et al.*: 2002, *Solar Phys.*, this volume.
Lin, R. P. *et al.*: 2002, *Solar Phys.*, this volume.
Smith, D. M. *et al.*: 2002, *Solar Phys.*, this volume.